Coiled-coil registry shifts in the F684I mutant of Bicaudal result in cargo-independent dynein recruitment

Heying Cui[1], Kathleen M. Trybus[2], M. Yusuf Ali[2], Puja Goyal[1], Xavier D. Aura[1], Jia Ying Loh[1], Sozanne R. Solmaz[1,*]

[1]Department of Chemistry, State University of New York at Binghamton, PO Box 6000, Binghamton, NY 13902. [2]Department of Molecular Physiology & Biophysics, University of Vermont, Burlington VT 05405.

Running title: *Structure of the Bicaudal mutant*

Cui ORCID 0000-0002-7244-9670
Trybus ORCID 0000-0002-5583-8500
Ali ORCID 0000-0003-2164-3323
Goyal ORCID 0000-0002-5812-0481
Solmaz ORCID 0000-0002-1703-3701

[*]To whom the correspondence should be addressed: Sozanne R Solmaz, Department of Chemistry, State University of New York at Binghamton, PO Box 6000, Binghamton NY 13902, ssolmaz@binghamton.edu, +1 607 777 2089.

Keywords: dynein, adaptor protein, Bicaudal, motor, auto-inhibition, coiled-coil registry shift, Nup358, crystallography, single-molecule biophysics, intracellular trafficking

ABSTRACT

Dynein adaptors such as *Drosophila* Bicaudal (*Dm* BicD) recognize cargo and are required to activate dynein for processive transport. In the absence of cargo, auto-inhibited BicD cannot recruit dynein, but the underlying mechanism of cargo-induced activation is elusive. We show with single molecule processivity assays that auto-inhibition is abolished in the full-length Bicaudal mutant F684I, which activates dynein motility even in the absence of cargo. To investigate the structural basis for activation, we determined the X-ray structure of the C-terminal cargo-binding domain (CTD) of *Dm* BicD-CTD/F684I. The mutant has a homotypic coiled-coil registry, in which the two helices of the homo-dimer are aligned at equal height. An N-terminal ~20 residue region is disordered for one of the two chains, and therefore the coiled-coil registry in that region cannot be assigned. The F684I mutation thus results in the formation of multiple conformations and induces flexibility. In contrast, the wild type structure has an asymmetric coiled-coil registry, in which the two chains are vertically shifted by ~ one helical turn in a portion of the coiled-coil. We propose that a coiled-coil registry shift upon cargo binding activates BicD for dynein recruitment. Interestingly, the human homolog of the Bicaudal mutant, BicD2-CTD/F743I, shows diminished binding of the cargo Nup358 compared with the wild type, while binding of the cargo Rab6^{GTP} is unaffected. Therefore, we propose that a coiled-coil registry shift also modulates cargo selection for BicD2–dependent transport pathways in *mammaliae*, which are important for brain development, faithful chromosome segregation and signaling.

Cytoplasmic dynein, the predominant minus-end directed microtubule motor, facilitates a vast number of cellular transport events (1). Dynein adaptor proteins, such as *Drosophila* Bicaudal (*Dm* BicD) (2) recognize cargo for dynein-dependent transport. Cargo-bound adaptors are required to activate metazoan dynein for processive transport and are therefore an essential part of the dynein transport machinery (3-8). In the

absence of cargo, BicD forms an auto-inhibited looped conformation, in which the C-terminal cargo binding region (CTD) binds to the N-terminal dynein/dynactin-binding site (coiled-coil domain 1, CC1), sterically preventing motor binding (3-12). The CTD is required for auto-inhibition, since a truncated BicD-CC1 construct without it activates dynein for processive transport in the absence of cargo (5,7). Auto-inhibition of full-length BicD is released upon cargo binding (3-12); however, the underlying molecular mechanism is elusive.

Notably, auto-inhibition is compromised in the classical *Dm* BicD Bicaudal mutant F684I, which recruits larger amounts of dynein from cell extracts compared to wild-type *Dm* BicD (9). The mutation causes dynein and Egalitarian-dependent mRNA transport defects and subsequent anterior accumulation of the *Oskar* mRNA pool (13-16), which result in a classical developmental phenotype that includes double-abdomen flies (9,13,17,18). Therefore, the Bicaudal mutant could potentially serve as a tool to investigate the molecular mechanism of BicD-auto-inhibition.

The most well characterized cargoes for *Dm* BicD are Egalitarian (19) and $Rab6^{GTP}$, which facilitate transport of mRNAs and Golgi-derived vesicles, respectively (20). The predominant cargoes for the human homologs Bicaudal D2 (*Hs* BicD2) and Bicaudal D1 (*Hs* BicD1) are $Rab6^{GTP}$ (20), which engages in the transport of Golgi-derived and secretory vesicles, and nuclear pore complex protein Nup358, which engages in transport of the cell nucleus (21-24). BicD2-dependent transport pathways are important for faithful chromosome segregation, neurotransmission at synapses, and essential for brain development (21-24). Mutations of BicD2 cause the neuromuscular disease spinal muscular atrophy (25-27). Cargo selection for BicD2-dependent transport is regulated by cargo competition (28), as well as the G2 phase specific kinase Cyclin-dependent kinase 1 (Cdk1) (21), however, additional regulatory mechanisms remain to be identified in order to explain how BicD2 switches from selecting Rab6-positive vesicles for transport in G1/S phase to recruiting dynein to the cell nucleus via Nup358 in G2 phase.

Cargo binds to the C-terminal domain (CTD) of *Dm* BicD (2), and the structure of the *Dm* BicD-CTD (9) as well as its homologs *Hs* BicD2 (29) and mouse (*Ms*) BicD1 (10) were determined, which all form homodimeric coiled-coils. Interestingly, *Hs* BicD2 and *Ms* BicD1 form a conformation with homotypic coiled-coil registry, in which the helices are aligned at equal height and the same residues from both chains engage in layers of knobs-into-holes interactions (10,29). In contrast, *Dm* BicD has an asymmetric coiled-coil registry. In the N-terminal half of the CTD, the helices are vertically shifted by ~1 helical turn respective to each other (heterotypic coiled-coil registry), whereas in the C-terminal half, the chains are aligned in a homotypic coiled-coil registry (9). Coiled-coil registry shifts have so far only been reported for a few proteins, including dynein (29-38), but may potentially be an inherent property of many coiled-coil structures with important physiological functions. In the case of BicD2, a coiled-coil registry shift may relieve auto-inhibition.

We recently used molecular dynamics (MD) simulations to probe structural dynamics in the BicD2-CTD coiled-coil (29). These simulations support the idea that BicD2 can adopt both a homotypic coiled-coil registry, and an asymmetric registry, as both states are similarly stable in simulations and defined by distinct conformations of F743 and F750, which stabilize either a homotypic or asymmetric coiled-coil registry (29). Notably, mutation of F743 to Ile (F684I in *Dm*) increases dynein recruitment in the *Drosophila* homolog compared to the wild type (9). In our MD simulations of the F743I mutant of *Hs* BicD2-CTD, a spontaneous coiled-coil registry shift from asymmetric to fully heterotypic coiled-coil registry was observed (29). We thus hypothesized that a coiled-coil registry shift upon cargo binding could relieve BicD-auto-inhibition and activate it for dynein recruitment, as has also been proposed earlier (9,10,29). In addition, in MD simulations of the R747C human disease mutant of *Hs* BicD2-CTD which causes spinal muscular atrophy, a spontaneous transient coiled-coil registry shift was observed, which may be an underlying cause of the disease (29).

Here we show that the Bicaudal mutation F684I abolishes auto-inhibition and allows cargo-independent recruitment of dynein. To investigate the structural basis for this activation, we determined the x-ray structure of the C-terminal cargo-binding domain (CTD) of *Dm* BicD-

CTD/F684I. Our data support the idea that the mutation induces a shift to a homotypic coiled-coil registry. Furthermore, the region N-terminal of F684I is disordered for one chain in the mutant structure, suggesting that the mutation renders the coiled-coil flexible, likely resulting in formation of multiple conformations.

RESULTS

The F684I mutation abolishes auto-inhibition of full-length Dm BicD.

A single molecule TIRF (Total Internal Reflectance Fluorescence) microscopy processivity assay was used to assess the functional properties of reconstituted dynein-dynactin-BicD (DDB) complexes. Complexes were reconstituted with either full-length *Dm* BicD ($BicD^{WT}$), full-length *Dm* BicD/F684I ($BicD^{F684I}$), or the truncated N-terminal fragment of *Dm* BicD ($BicD^{CC1}$). The molar ratio of dynein-dynactin:BicD was 1:2 to ensure recruitment of only 1 dynein to the ternary complex (11). Full-length WT *Dm* BicD is auto-inhibited and does not recruit dynein-dynactin, while the truncated N-terminal fragment fully activates dynein-dynactin for processive transport (5,7,11,12). Consistent with previous results (11), we did not observe processive directional movement for DDB^{WT} on microtubule tracks, although some one-dimensional diffusive events of the Qdot-labeled dynein were observed. Because DDB^{WT} showed no directional motion (Movie S1), speed and run length were not measured. In contrast, DDB^{CC1} showed robust processivity, which was indistinguishable from that observed with DDB^{F684I} (Fig. 1A,B, Movie S2 and S3). The speeds of both DDB^{CC1} and DDB^{F684I} were fitted with a single Gaussian (Fig. 1C). The DDB^{F684I} complex moved at a speed of 0.43 ± 0.17 µm/s (n=68), which was not significantly different (p=0.44) from what was observed for DDB^{CC1} (0.41 ± 0.21 µm/s, n=58). Processive run-lengths were fitted with a standard exponential decay equation ($y= Ae^{-bx}$), where A is the amplitude and 1/b is run length. The run length of DDB^{F684I} (3.3 ± 0.18 µm, n=68) was not significantly different (p=0.9) from that of DDB^{CC1} (2.8 ± 0.13 µm, n=58) (Fig. 1D).

Based on run frequency, speed and processive run length, we conclude that the full-length mutant *Dm* BicD/F684I was not auto-inhibited and was fully capable of binding and activating dynein-dynactin for processive transport in the absence of cargo.

Crystal structure of the Dm BicD-CTD/F684I mutant provides mechanistic insights into cargo-independent activation.

To gain structural insights into the molecular mechanism of activation of BicD, we determined the structure of the C-terminal domain of *Drosophila melanogaster* BicD/F684I (*Dm* BicD-CTD/F684I, residues 656-745). Crystals were obtained in the space group $P3_1$ 2 1. The structure was determined by molecular replacement in the PHENIX suite (39), using coordinates from the wild-type structure (9) that were truncated N-terminal of residue 692 as the search model. The structure was refined to 2.35Å resolution, with an R_{free} of 25.99% and an R_{work} of 25.06% (Table 1). In the structure, *Dm* BicD-CTD/F684I forms a homo-dimeric coiled-coil. However, in contrast to the structure of the wild type, in the structure of the Bicaudal mutant, a ~20 residue N-terminal region upstream of the mutated residue I684 is not resolved in the electron density map for one chain of the dimer (Fig. 2). However, the same region is well defined in the electron density map for the second chain. Consequently, the model contains residues 666-740 and 684-741 for the two chains, respectively.

Coiled-coils such as *Dm* BicD-CTD are characterized by heptad repeats 'abcdefg' in the sequence, where residues at 'a' and 'd' positions are predominantly hydrophobic. These residues form characteristic "knobs-into-holes interactions", where a knob from one chain (either an 'a' or 'd' position residue) fits into a hole formed of four residues on the opposite chain (40,41). Notably, structures of distinct BicD homologs with distinct coiled-coil registries have been determined. *Hs* BicD2-CTD has a homotypic coiled-coil registry, with characteristic layers of knobs-into-holes interactions, which are formed by the same knob residues from both chains, and therefore the helices are aligned at equal height. Wild-type *Dm* BicD-CTD (Fig. 2A) however has an asymmetric coiled-coil registry. The N-terminal half of the coiled-coil has a heterotypic registry, in which residue *i* from one chain is paired up with residue *i*+4 from the second chain to form layers

of knobs-into-holes interactions, resulting in a vertical displacement of the helices by ~one helical turn. In the C-terminal half, the helices are aligned to form a coiled-coil with homotypic registry.

To determine the coiled-coil registry, we assigned the heptad register of the structure of *Dm* BicD-CTD/F684I. (Fig. 2, Fig. S1). As observed for the wild-type *Dm* BicD-CTD (Fig. 2A) and *Hs* BicD2-CTD (Fig. 2C), the C-terminal half of the mutant structure has a homotypic coiled-coil registry (Fig. 2B, see Table 2 for residue numbering in *Hs* and *Dm* homologs). Notably, one additional layer of knobs-into-holes interactions with homotypic coiled-coil registry was identified in the Bicaudal mutant compared to the *Dm* BicD wild type. This layer is formed by knob residue V702 from both chains (Fig. 2, Fig. S1). In contrast to the F684I mutant, in the *Dm* BicD wild type, V702 forms a layer of knobs-into-holes interactions with residue Y698 and therefore part of the region that has a heterotypic coiled-coil registry. Wild-type *Dm* BicD-CTD also has additional layers of knob-into-holes interactions with heterotypic registry in its N-terminal region, resulting in a vertical displacement of the helices by approximately one helical turn. However, no additional layers of knobs-into-holes interactions N-terminal of V702 were identified in the structure of *Dm* BicD-CTD/F684I, because a ~20 residue region upstream of residue I684 is not resolved for one chain (Fig. 2).

A least-squares superimposition of the structures of the *Dm* BicD-CTD/F684I mutant and the wild type revealed that in the mutant, both I684 residues are aligned at equal height, as observed for the homologous residue F743 in *Hs* BicD2 with homotypic registry (Fig. 2 D-G). However, in the wild-type *Dm* BicD structure, which has an asymmetric coiled-coil registry, residues F684 from both chains are vertically shifted by approximately one helical turn with respect to each other (Fig. 2 D-G). F684 from one chain lines up with R688 from the second chain to form a layer of knobs-into-holes interactions (heterotypic registry) (Fig. 2A).

To conclude, several pieces of data suggest that the structure of the *Dm* BicD2-CTD/F684I mutant has a homotypic coiled-coil registry: One additional layer of knobs-into-holes interactions with homotypic coiled-coil registry is formed by residues V702 in the structure of the Bicaudal mutant compared to the wild type. Furthermore, residues I684 are aligned in the structure of the Bicaudal mutant at equal height (homotypic registry), whereas in the wild type, residues F684 are vertically shifted respectively to each other by approximately one helical turn (heterotypic registry). However, since a ~20 residue area of one monomer in the Bicaudal mutant is not resolved, no additional knobs-into-holes interactions were identified, therefore, the coiled-coil registry N-terminal of I684 is unknown.

Distinct conformations of F684 and F691 stabilize distinct coiled-coil registries.

Another key residue that is important to stabilize either a homotypic or asymmetric coiled-coil registry is F691 (Fig. 3). In the *Dm* BicD-CTD wild type structure with the asymmetric coiled-coil registry, phenylalanine side chains of F691 from both chains interact in a face-to-edge aromatic interaction, which leads to vertical displacement of the chains by ~1 helical turn (Fig. 3B). However, in the BicD homologs with homotypic registry (*Ms* BicD1, *Hs* BicD2) the homologous phenylalanine residues interact with face-to-face aromatic interaction, which allows the chains to be aligned in the homotypic registry (Fig. 3D, E). In the *Dm* BicD F684I mutant, the phenylalanine side chains of F691 from both chains interact face-to-face (Fig. 3A, C, F), which suggests a homotypic registry. A least-squares superimposition of the structures of the *Dm* BicD wild type and the F684I mutant confirms that the F691 side chains form a face-to-face aromatic interaction in the structure of the Bicaudal mutant and a face-to-edge aromatic interaction in the wild type with the asymmetric registry (Fig. 3C). These data suggest that in the structure of the *Dm* BicD F684I mutant, the F691 residues assume a conformation that is found in *Hs* BicD2 with homotypic coiled-coil registry.

The disordered region is present in the crystal, and α-helical.

Because a ~20 residue region of one chain is not resolved in the crystal structure, we dissolved crystals of *Dm* BicD-CTD/F684I and analyzed them by SDS-PAGE, to assess whether the crystals contained the intact protein (Fig. 4A). A comparison of the SDS-PAGE of the dissolved

crystals, the purified *Dm* BicD-CTD/F684I protein as well as the wild-type protein suggests that indeed the intact *Dm* BicD-CTD/F684I protein is present in crystal, suggesting that the unresolved N-terminal region is disordered.

In order to assess, whether the disordered portion of the helix is α-helical (rather than misfolded), we probed the secondary structure content of *Dm* BicD-CTD/F684I by circular dichroism (CD) wavelength scans. The CD wavelength spectra of the *Dm* BicD-CTD/F684I mutant and the wild type both have minima at 208nm and 222nm, which are characteristic of α-helical proteins. Notably, the spectra of the F684I mutant and the wild type overlay perfectly, suggesting that both structures have a very similar α-helical content. These data suggest that the ~20 residue disordered region is α-helical rather than unstructured (Fig. 4B).

Furthermore, we compared the dimer interface of the structure of the F684I mutant with the wild type (Table S1). Since the N-terminal region of one of two chains is disordered in the mutant, the interface area is smaller (1427 $Å^2$) compared to the wild type (1764 $Å^2$), and the dimer interface of the F684I mutant contains eighteen fewer interacting residues as well as one less hydrogen bond and one less salt bridge compared to the wild type (Table S1). It is unknown if the disordered region engages in interactions that stabilize the dimer, however, in the absence of additional interactions one would expect that the F684I mutant would be less stable than the wild type.

Thus, we probed thermodynamic stability of the F684I mutant and the wild type by recording circular dichroism spectroscopy melting curves (Fig. 4C). Protein unfolding was monitored by CD spectroscopy at 222 nm. The apparent melting temperature T_M of *Dm* BicD-CTD/F684I was 45.2±1.4°C, which is similar to the T_M of the wild type protein (42.3±0.6°C) (Fig. 4C). Based on the melting temperatures, the *Dm* BicD-CTD/F684I mutant has comparable thermodynamic stability as the wild type, despite the N-terminal disordered portion of one helix. Therefore, it is conceivable that the disordered portion still interacts with the other chain, as it would explain the observed similar thermodynamic stability.

To conclude, the ~20 residue disordered region is present in the crystal and folded, and since the thermodynamic stability of the mutant is comparable to the wild type, this region is likely to still interact with the other chain. These data suggest that the region N-terminal of I684 is flexible in the mutant in one chain and possibly assuming multiple conformations.

MD simulations suggest that a conformation of the mutant with homotypic registry is stable.

In the X-ray structure, the Bicaudal mutant of *Dm* BicD-CTD assumes a conformation with a homotypic coiled-coil registry, and the region N-terminal of F684I is disordered for one of two chains. In comparison, in our recent MD simulations of the human homolog of the Bicaudal mutant, *Hs* BicD2/F743I with asymmetric coiled-coil registry, the homologous F743I mutation induced a coiled-coil registry shift from an asymmetric to a fully heterotypic registry (29). Since the Bicaudal mutant has a homotypic coiled-coil registry in the X-ray structure, we used MD simulations to assess if a conformation of the mutant with a homotypic registry would be stable. For these simulations, the structure of the homolog *Hs* BicD2-CTD was chosen as a starting point, since it has a homotypic coiled-coil registry (unlike *Dm* BicD WT), and the homologous F743I mutation was introduced. In these simulations, the homotypic registry was preserved, suggesting that it is a stable conformation for the *Hs* BicD2-CTD/F743I (Fig. 5), consistent with the crystal structure.

It is conceivable that F743 is a key residue that serves to lock the BicD2 coiled-coil in conformations with either homotypic or asymmetric registry. Replacement of this residue by isoleucine may lead to promiscuity, allowing other conformations to form. This is in line with the crystal structure and the MD simulations. It should be noted that the structure has an elevated overall B-factor (Table 1), indicating flexibility, and a region of one chain that undergoes coiled-coil registry shifts is also disordered, further suggesting conformational variability.

To conclude, our MD simulations of the human homolog of the Bicaudal mutant show that conformations with homotypic registry or fully heterotypic registry are both stable, whereas a conformation with asymmetric registry is not stable (29) (Fig. 5).

The homologous F743I mutation modulates cargo selection in Hs BicD2.

Because a registry shift is expected to re-model the surface of the coiled-coil, which harbors binding sites for cargoes, we investigated whether a coiled-coil registry shift in BicD2 plays a role in cargo selection. Cargo binding sites have been previously mapped (9,10). The cargo binding sites for *Dm* Egalitarian and *Dm* Rab6^{GTP} on *Dm* BicD have been mapped to residues 702-743 (Fig. 6A). A similar region has been mapped as minimal Rab6^{GTP} cargo binding site for a close homolog of human BicD2 (residues 755-802, Fig. 6B, see Table 2 for residue numbering in *Dm* and *Hs* homologs). These cargoes bind to the C-terminal homotypic region of *Dm* BicD-CTD/ *Hs* BicD2-CTD, which does not undergo coiled-coil registry shifts and therefore a coiled-coil registry shift is not expected to alter cargo binding. Indeed, the F684I mutant of *Drosophila* BicD does not affect the interaction of BicD with its cargoes Egalitarian and Rab6^{GTP} (9).

Notably, the mammalian cargo Nup358 binds to a larger region that includes residues 724-802 of *Hs* BicD2 (mapped for a homolog) (10). A portion of this region undergoes a coiled-coil registry shift (Fig. 6B). Several important Nup358 interface residues, which are N-terminal of F743 were identified for a close homolog of human BicD2 (Table 2; residues L746, R747, M749 and R753). Mutation of each of these residues to alanine strongly diminishes the interaction (10).

We therefore hypothesized that the homologous F743I mutation in *Hs* BicD2 would modulate the interaction between BicD2 and Nup358, since a portion of the interface is located in the region that is thought to undergo coiled-coil registry shifts. The BicD2/Rab6^{GTP} interaction however is expected to be unaffected by the F743I mutation, since the binding site is located in the region that remains homotypic. This is confirmed by a pull-down assay of Rab6^{GTP} with the BicD2-CTD/F743I mutant, which binds with comparable strength as the wild type (Fig. 6C). Interestingly, cargo selection for Nup358 is modulated by the mutation. In a pull-down-assay, the minimal interacting domain Nup358-min pulls down wild-type BicD2-CTD much more strongly compared to the F743I mutant (Fig. 6D). Binding is even more strongly weakened for the double mutant F743I/R747C, which combines two mutations that induced coiled-coil registry shifts in simulations (Fig. 6E) (29).

To gain further insights into the impact of the mutation on the cargo-binding interface, we compared the electrostatic surface potential of the structures of *Dm* BicD-CTD/F684I, the wild type (asymmetric registry), and *Hs* BicD2-CTD (homotypic registry) (Fig. 6F-I). There are differences in the electrostatic surface potential in the area where Nup358 binds (L746, R747, M749 and R753 (10) (Fig. 6F-I). Notably, both the Bicaudal mutant BicD-CTD/F684I and *Hs* BicD2-CTD (homotypic registry) have a highly positively charged surface electrostatic potential in the area of these interface residues, creating a basic pocket (blue, Fig. 6G,I). In comparison, the same interface area in the *Dm* BicD-CTD has a much less charged electrostatic surface potential (Fig. 6H). Such changes could be caused by a coiled-coil registry shift and could be responsible for the observed difference for the interaction between *Hs* BicD2-CTD wild type and the F743I mutant with Nup358-min.

To conclude, while the *Dm* BicD F684I mutant shows comparable selectivity as the wild type protein towards the cargoes Egalitarian and Rab6^{GTP} (9), in human BicD2, the homologous F743I mutant which likely induces a coiled-coil registry shift affects cargo selection. While binding of BicD2 to Rab6^{GTP} is not affected by the mutation, binding to Nup358 is strongly reduced, likely because it binds to a larger binding site that contains a portion of the protein that may undergo a coiled-coil registry shift.

DISCUSSION

In the absence of cargo, BicD forms an auto-inhibited state that is unable to recruit dynein (3-12). Here we show by single molecule processivity assays that auto-inhibition is abolished in the classical Bicaudal mutant BicD/F684I, resulting in cargo-independent activation of dynein-dynactin, consistent with cellular studies that show increased dynein recruitment (9,13). To probe the mechanism of BicD activation from the auto-inhibited state, we determined the X-ray structure of the C-terminal cargo-binding domain of the Bicaudal mutant (*Dm* BicD-CTD/F684I). The Bicaudal mutant assumes a conformation with homotypic registry as its predominant structural state, as the helices are aligned at equal height up

to residue I684, unlike in the wild-type, where F684 residues are displaced vertically by one helical turn against each other.

It was previously proposed that BicD undergoes coiled-coil registry shifts, which activate it for dynein recruitment upon cargo binding (9,10,29). This idea is based on structures of distinct BicD homologs with distinct coiled-coil registries as well as our recent MD simulations, which suggest that human BicD2 can assume stable conformations with either homotypic or asymmetric coiled-coil registries (9,10,29). Notably, in these simulations, the F743I mutation (the human homolog to the *Dm* mutant F684I) induced a spontaneous coiled-coil registry shift in human BicD2 (29). Results from our MD simulations suggest that conformations with heterotypic and homotypic registries of the Bicaudal mutant are stable, while a conformation with an asymmetric registry is not stable. These results also suggest that the mutation induces structural dynamicity, and leads to formation of multiple conformations, which is also supported by the crystal structure. The structure has a comparatively high B-factor, suggesting flexibility and a ~20 amino acid region at the N-terminus of one chain is not resolved in the structure, whereas the second chain is resolved, and therefore the coiled-coil registry in this region cannot be determined. Our data suggest that the disordered region is present in the crystal and α-helical. The disordered region likely also still interacts with the second ordered chain in the crystal, since the melting temperatures indicate similar thermodynamic stability for the mutant and the wild type.

In the wild type, F684 likely serves as a switch to lock *Dm* BicD in conformations with distinct registries (9,29). In the conformation with the asymmetric registry, F684 rotates to the core of the coiled-coil and forms an edge-to-face aromatic interaction with residue F684 from the second chain, which leads to the observed vertical displacement of the helices (9,29). In the mutant, the phenylalanine side chain is replaced by a much smaller isoleucine side chain, which likely cannot lock the asymmetric registry in place, and due to its smaller size is unable to prevent conformational changes. The result is likely a dynamic mixture of several states.

The single molecule assays, which use full-length mutant BicD, are consistent with the predictions derived from the minimal cargo-binding domain structure. In the auto-inhibited conformation, full-length BicD2 forms a looped structure in which the CTD binds to the N-terminal dynein/dynactin binding site, likely causing steric interference (3-12). Cargo binding could induce a local coiled-coil registry shift in the BicD2-CTD, which might be sufficient to weaken binding to the N-terminal dynein/dynactin binding site and thus activate BicD for dynein recruitment. Alternatively the registry shift could propagate through the entire coiled-coil to the N-terminal dynein-dynactin binding site. Furthermore, the induced flexibility and formation of multiple conformations as observed in the mutant may potentially also be an inherent structural feature of cargo-bound wild type BicD. Such structural and mechanistic details remain to be established and studies with full-length proteins in physiological context remain to be conducted to fully understand the molecular mechanism of BicD2 auto-inhibition and activation.

In addition to BicD2, several other dynein adaptors have coiled-coil structures (e.g. NudE/NudEL (42-44), the Hook proteins (45,46), RILP (47), Rab11-FIP3 and Spindly (48,49)) and some of them, e.g. Spindly assume an auto-inhibited state in the absence of cargo (7,49). The molecular mechanism for auto-inhibition in these dynein adaptors remains to be established, and it is possible that some of them undergo coiled-coil registry shifts as well.

Notably, we propose that coiled-coil registry shifts in human BicD2 modulate cargo selection. In *Drosophila*, Egalitarian and $Rab6^{GTP}$ bind to a smaller domain of BicD that remains homotypic and does not undergo coiled-coil registry shifts, consistent with the Bicaudal mutation not affecting cargo selection (9,19). However, human Nup358 binds to a larger interface on BicD2 that includes a region which undergoes coiled-coil registry shift (10). The homologous F743I mutation which is expected to induce a coiled-coil registry shift (29) diminishes binding of Nup358 to *Hs* BicD2, whereas the interaction of BicD2 with $Rab6^{GTP}$ is unaffected. Cargo selection for BicD2-dependent transport events are tightly regulated, but currently known regulatory mechanisms, which include cargo competition (28) and the G2 specific kinase

Cdk1 (21), are insufficient to fully explain how BicD2 switches between these cargoes in a cell-cycle specific manner (28). A coiled-coil registry shift in BicD2 could be triggered by a regulatory mechanism, modulating cargo selection for these transport pathways.

In conclusion, our data provide mechanistic insights into auto-inhibition and cargo selection of the dynein adaptor BicD2. Our results suggest that the full-length *Dm* BicD/F684I mutant is capable of activating dynein for processive transport in a cargo-independent manner. The X-ray structure of *Dm* BicD-CTD/F684I reveals that the mutation induces a coiled-coil registry shift, which we propose as the underlying mechanism for cargo-independent activation. A ~20 residue N-terminal region of one monomer is disordered, and this observed structural dynamicity could either be a structural feature of activated BicD2 or it could be caused by the mutation. Notably, the human homolog of the Bicaudal mutant shows reduced affinity to the cargo Nup358. We thus propose that a coiled-coil registry shift modulates cargo selection for BicD2-dependent transport pathways, which are important for cell cycle control and brain development (19,21-24,50).

EXPERIMENTAL PROCEDURES

Protein expression and purification

Dynein was expressed with an N-terminal biotin tag in Sf9 cells and dynactin was purified from bovine brain tissue as described (11). Full-length *Drosophila* BicD WT ($BicD^{WT}$) and BicD/F684I ($BicD^{F684I}$) were expressed in Sf9 cells and BicD-coiled-coil domain 1 ($BicD^{CC1}$) in bacteria as described (11).

To create an expression construct of *Drosophila* BicD-CTD/F684I (residues 656-745), the corresponding codon optimized DNA sequence was commercially synthesized by Genscript and cloned into the pET28a vector with the NdeI and XhoI restriction sites. *Drosophila* Bicaudal D-CTD F684I (*Dm* BicD-CTD F684I, residues 656-745) was expressed in E. *coli* BL20(DE3)-RIL strain. His_6-tagged *Dm* BicD-CTD/F684I was purified by Ni-NTA affinity chromatography and the tag was cleaved by thrombin, followed by second Ni-NTA affinity chromatography as described in (28). The protein was further purified by gel filtration chromatography on a HiLoad™ 16/600 Superdex 200 pg column (GE Healthcare) with the following buffer: 20 mM HEPES pH 7.5, 150 mM NaCl, 0.5 mM TCEP as described (28). Wild-type *Dm* BicD-CTD was expressed and purified as described (29). Purified protein was analyzed by SDS-PAGE, 16% acrylamide gels and stained by Coomassie Blue. GST-pull down assays were performed as described (29).

Crystallization

Purified *Dm* BicD-CTD/F684I was set up for crystallization in hanging drops. Crystals in space group $P3_121$ were obtained after 2-3 days in the dimensions 0.2 mm * 0.2 mm * 0.2 mm. Crystals were soaked in a cryobuffer and flash frozen in liquid nitrogen.

Structure determination

Data was collected from a single crystal at NE-CAT beam line 24ID-C at the Advanced Photon Source (APS), Argonne National Lab (ANL), which was equipped with a Pilatus 6M detector. X-ray intensities were processed and scaled using the RAPD software developed by F. Murphy, D. Neau, K. Perry and S. Banerjee, APS (https://rapd.nec.aps.anl.gov/login/login.html).
The structure was determined by molecular replacement in the PHENIX suite (39), with the structure of the wild-type as the search model, which was truncated N-terminal of residue 692 (9). An initial model was obtained from automatic model building in the PHENIX suite and completed by manual model building in the program COOT (39,51). The structure was refined through iterative cycles of manual model building and refinement (39,51) to 2.35Å resolution in the PHENIX suite (39), with an R_{free} of 25.99% and an R_{work} of 25.06% (Table 1). The stereochemical quality of the model was assessed with MolProbity (52). The crystallographic statistics are summarized in Table 1.

Structural analysis

Structures were compared by least-squares superimposition of the coordinates in COOT (51). Dimer interfaces and knobs-into-holes interactions were analyzed by the web servers PISA and SOCKET, respectively (53,54) . For identification of knobs-into-hole interactions, a cutoff of 7.5 Å was used (helix extension 1 residue). Figures were

created in the PyMOL Molecular Graphics System, Version 2.0 (Schrödinger, LLC) and VMD (55). The program APBS was used to analyze surface electrostatic potentials of proteins (56). Default parameters were used; neutral charges were assigned to the N- and C-termini, waters were removed and selenomethionine residues were converted to methionine.

Single molecule processivity assays with full-length *Dm* BicD

The motility assay was performed on PEGylated slides using a buffer containing 30 mM HEPES pH 7.4, 50 mM KOAc, 2 mM MgOAc, 1 mM EGTA, 2 mM MgATP, 20 mM DTT, 8 mg/ml BSA, 0.5 mg/ml k-casein, 0.5% pluronic F68, 10 mM paclitaxel and an oxygen scavenger system (5.8 mg/ml glucose, 0.045 mg/ml catalase, and 0.067 mg/ml glucose oxidase (11). Total Internal Reflectance Fluorescence (TIRF) microscopy was used to capture images of Qdot labeled dynein. Imaging was performed a Nikon ECLIPSE Ti microscope equipped with through-objective type TIRF and run by the Nikon NIS Elements software. Images were captured at 200 ms temporal and 6 nm spatial resolution. The Qdot(655nm)-labeled dynein and rhodamine-labeled microtubules were excited with the 488 and 651 nm laser lines and images simultaneously recorded at five frames/s using two Andor EMCCD cameras (Andor Technology USA, South Windsor, CT). Run-length was total travel distance, and speed was total travel distance divided by time. Binding frequency was normalized to number of events per time per µm microtubule. For statistical significance, an unpaired t-test with 95% confidence interval was performed for the speed data. For run length data, the Kolmogorov-Smirnov test with a 95% confidence interval was performed.

Molecular dynamics simulations

MD simulations with implicit solvent were carried out using the CPU implementation of the PMEMD program in the AMBER16 package (57) as described (29). The use of an implicit solvent model was justified by comprehensive comparisons of the results to those from explicit solvent simulations.

CD spectroscopy

Purified *Dm* BicD-CTD/F684I (0.3 mg/ml) was dialyzed in the following buffer: 500 mM NaCl, 10 mM Tris pH 8 and 0.2 mM TCEP. CD spectra were recorded with a Jasco J-810 CD Spectrometer equipped with a thermoelectric control device, using a cuvette with a path length of 0.1cm. After the buffer baseline subtraction, CD signals were normalized to the protein concentration and converted to mean residue molar ellipticity [Θ]. CD spectra from 190 to 260nm were measured at 4°C or 90°C as described (29). Thermal unfolding profiles of proteins were recorded by CD spectroscopy at 222 nm as described (29).

ACKNOWLEDGMENTS
This paper was supported by the following grants: National Institute of Health, National Institute of General Medical Sciences (NIH NIGMS) grant 1R15GM128119-01 awarded to S.R.S. and GM078097 to KMT. Additional funds came from the Chemistry Department at State University of New York at Binghamton and the Research Foundation of the State University of New York.
X-ray diffraction data was collected at Northeastern Collaborative Access Team (NE-CAT) beam line 24ID-C at the Advanced Photon Source (APS), Argonne National Lab (ANL), which are funded by the National Institute of General Medical Sciences from the National Institutes of Health (P30 GM124165) and by a NIH-ORIP HEI grant (S10 RR029205). APS is operated by ANL for the DOE under contract No. DE-AC02-06CH11357. We thank Jonathan P Schuermann from APS and Richard Vallee from Columbia University for helpful discussions. We also thank Carol Bookwalter and Elena Krementsova for cloning, protein expression and protein purification. This work used the Extreme Science and Engineering Discovery Environment (XSEDE)(58), which is supported by NSF grant ACI-1548562. All figures related to the computational studies were made using the Visual Molecular Dynamics (VMD) program (55). Furthermore, we thank S. Bane & B. Callahan (SUNY Binghamton), for access to equipment. Coordinates and structure factors were deposited to the protein data bank (PDB ID 6TZW). The content is solely the responsibility of the authors and does not necessarily represent the official views of the National Institutes of Health.

CONFLICTING INTERESTS
The authors declare that they have no conflicting interests.

REFERENCES

1. Cianfrocco, M. A., DeSantis, M. E., Leschziner, A. E., and Reck-Peterson, S. L. (2015) Mechanism and regulation of cytoplasmic dynein. *Annu Rev Cell Dev Biol* **31**, 83-108
2. Hoogenraad, C. C., Akhmanova, A., Howell, S. A., Dortland, B. R., De Zeeuw, C. I., Willemsen, R., Visser, P., Grosveld, F., and Galjart, N. (2001) Mammalian Golgi associated Bicaudal D2 functions in the dynein dynactin pathway by interacting with these complexes. *EMBO J* **20**, 4041-4054
3. Splinter, D., Razafsky, D. S., Schlager, M. A., Serra-Marques, A., Grigoriev, I., Demmers, J., Keijzer, N., Jiang, K., Poser, I., Hyman, A. A., Hoogenraad, C. C., King, S. J., and Akhmanova, A. (2012) BICD2, dynactin, and LIS1 cooperate in regulating dynein recruitment to cellular structures. *Mol Biol Cell* **23**, 4226-4241
4. Schlager, M. A., Serra-Marques, A., Grigoriev, I., Gumy, L F., Esteves da Silva, M., Wulf, P S., Akhmanova, A., and Hoogenraad, C C. (2014) Bicaudal D family adaptor proteins control the velocity of dynein-based movements. *Cell Rep* **8**, 1248-1256
5. Schlager, M. A., Hoang, H. T., Urnavicius, L., Bullock, S. L., and Carter, A. P. (2014) In vitro reconstitution of a highly processive recombinant human dynein complex. *EMBO J* **33**, 1855-1868
6. Urnavicius, L., Zhang, K., Diamant, A. G., Motz, C., Schlager, M. A., Yu, M., Patel, N. A., Robinson, C. V., and Carter, A. P. (2015) The structure of the dynactin complex and its interaction with dynein. *Science* **347**, 1441-1446
7. McKenney, R. J., Huynh, W., Tanenbaum, M. E., Bhabha, G., and Vale, R. D. (2014) Activation of cytoplasmic dynein motility by dynactin-cargo adapter complexes. *Science* **345**, 337-341
8. Chowdhury, S., Ketcham, S. A., Schroer, T. A., and Lander, G. C. (2015) Structural organization of the dynein-dynactin complex bound to microtubules. *Nat Struct Mol Biol* **22**, 345-347
9. Liu, Y., Salter, H. K., Holding, A. N., Johnson, C. M., Stephens, E., Lukavsky, P. J., Walshaw, J., and Bullock, S. L. (2013) Bicaudal-D uses a parallel, homodimeric coiled coil with heterotypic registry to coordinate recruitment of cargos to dynein. *Genes Dev* **27**, 1233-1246
10. Terawaki, S., Yoshikane, A., Higuchi, Y., and Wakamatsu, K. (2015) Structural basis for cargo binding and autoinhibition of Bicaudal-D1 by a parallel coiled-coil with homotypic registry. *Biochem Biophys Res Commun* **460**, 451-456.
11. Sladewski, T. E., Billington, N., Ali, M. Y., Bookwalter, C. S., Lu, H., Krementsova, E. B., Schroer, T. A., and Trybus, K. M. (2018) Recruitment of two dyneins to an mRNA-dependent Bicaudal D transport complex. *eLife* **7**, e36306
12. McClintock, M. A., Dix, C. I., Johnson, C. M., McLaughlin, S. H., Maizels, R. J., Hoang, H. T., and Bullock, S. L. (2018) RNA-directed activation of cytoplasmic dynein-1 in reconstituted transport RNPs. *eLife* **7**, e36312
13. Mohler, J., and Wieschaus, E. F. (1986) Dominant maternal-effect mutations of Drosophila melanogaster causing the production of double-abdomen embryos. *Genetics* **112**, 803-822
14. Navarro, C., Puthalakath, H., Adams, J. M., Strasser, A., and Lehmann, R. (2004) Egalitarian binds dynein light chain to establish oocyte polarity and maintain oocyte fate. *Nat Cell Biol* **6**, 427-435
15. Zimyanin, V. L., Belaya, K., Pecreaux, J., Gilchrist, M. J., Clark, A., Davis, I., and St Johnston, D. (2008) In vivo imaging of oskar mRNA transport reveals the mechanism of posterior localization. *Cell* **134**, 843-853
16. Mach, J. M., and Lehmann, R. (1997) An Egalitarian-BicaudalD complex is essential for oocyte specification and axis determination in Drosophila. *Genes Dev* **11**, 423-435
17. Bull, A. L. (1966) Bicaudal, a genetic factor which affects the polarity of the embryo in Drosophila melanogaster. *J Exp Zool* **161**, 221-241

18. Wharton, R. P., and Struhl, G. (1989) Structure of the Drosophila Bicaudal D protein and its role in localizing the posterior determinant nanos. *Cell* **59**, 881-892
19. Dienstbier, M., Boehl, F., Li, X., and Bullock, S. L. (2009) Egalitarian is a selective RNA-binding protein linking mRNA localization signals to the dynein motor. *Genes Dev* **23**, 1546-1558
20. Matanis, T., Akhmanova, A., Wulf, P., Del Nery, E., Weide, T., Stepanova, T., Galjart, N., Grosveld, F., Goud, B., De Zeeuw, C. I., Barnekow, A., and Hoogenraad, C. C. (2002) Bicaudal-D regulates COPI-independent Golgi-ER transport by recruiting the dynein-dynactin motor complex. *Nat Cell Biol* **4**, 986-992
21. Baffet, A D., Hu, D J., and Vallee, R B. (2015) Cdk1 activates pre-mitotic nuclear envelope dynein recruitment and apical nuclear migration in neural stem cells. *Dev Cell* **33**, 703-716
22. Hu, D. J., Baffet, A. D., Nayak, T., Akhmanova, A., Doye, V., and Vallee, R. B. (2013) Dynein recruitment to nuclear pores activates apical nuclear migration and mitotic entry in brain progenitor cells. *Cell* **154**, 1300-1313
23. Loftus, K. M., Coutavas, E., Cui, H., King, D., Ceravolo, A., Pereiras, D., and Solmaz, S. (2017) Mechanism for G2 phase-specific nuclear export of the kinetochore protein CENP-F. *Cell Cycle* **16**, 1414-1429
24. Splinter, D., Tanenbaum, M. E., Lindqvist, A., Jaarsma, D., Flotho, A., Yu, K. L., Grigoriev, I., Engelsma, D., Haasdijk, E. D., Keijzer, N., Demmers, J., Fornerod, M., Melchior, F., Hoogenraad, C. C., Medema, R. H., and Akhmanova, A. (2010) Bicaudal D2, dynein, and kinesin-1 associate with nuclear pore complexes and regulate centrosome and nuclear positioning during mitotic entry. *PLoS Biol* **8**, e1000350
25. Peeters, K., Litvinenko, I., Asselbergh, B., Almeida-Souza, L., Chamova, T., Geuens, T., Ydens, E., Zimon, M., Irobi, J., De Vriendt, E., De Winter, V., Ooms, T., Timmerman, V., Tournev, I., and Jordanova, A. (2013) Molecular defects in the motor adaptor BICD2 cause proximal spinal muscular atrophy with autosomal-dominant inheritance. *Am J Hum Gen* **92**, 955-964
26. Synofzik, M., Martinez-Carrera, L. A., Lindig, T., Schöls, L., and Wirth, B. (2014) Dominant spinal muscular atrophy due to BICD2: a novel mutation refines the phenotype. *J Neurol Neurosurg Psychiatry* **85**, 590-592
27. Martinez-Carrera, L. A., and Wirth, B. (2015) Dominant spinal muscular atrophy is caused by mutations in BICD2, an important golgin protein. *Front Neurosci* **9**, 401
28. Noell, C. R., Loftus, K. M., Cui, H., Grewer, C. T., Kizer, M., Debler, E. W., and Solmaz, S. R. (2018) A quantitative model for BicD2/cargo interactions. *Biochemistry* **57**, 6538-6550
29. Noell, C. R., Loh, J. Y., Debler, E. W., Loftus, K. M., Cui, H., Russ, B. B., Zhang, K., Goyal, P., and Solmaz, S. R. (2019) Role of Coiled-Coil Registry Shifts in the Activation of Human Bicaudal D2 for Dynein Recruitment upon Cargo Binding. *J Phys Chem Lett* **10**, 4362-4367
30. Macheboeuf, P., Buffalo, C., Fu, C.-y., Zinkernagel, A. S., Cole, J. N., Johnson, J. E., Nizet, V., and Ghosh, P. (2011) Streptococcal M1 protein constructs a pathological host fibrinogen network. *Nature* **472**, 64-68
31. Carter, A. P., Garbarino, J. E., Wilson-Kubalek, E. M., Shipley, W. E., Cho, C., Milligan, R. A., Vale, R. D., and Gibbons, I. R. (2008) Structure and functional role of dynein's microtubule-binding domain. *Science* **322**, 1691-1695
32. Gibbons, I. R., Garbarino, J. E., Tan, C. E., Reck-Peterson, S. L., Vale, R. D., and Carter, A. P. (2005) The Affinity of the Dynein Microtubule-Binding Domain is Modulated by the Conformation of its Coiled-Coil Stalk. *J Biol Chem* **280**, 23960-23965
33. Croasdale, R., Ivins, F. J., Muskett, F., Daviter, T., Scott, D. J., Hardy, T., Smerdon, S. J., Fry, A. M., and Pfuhl, M. (2011) An Undecided Coiled Coil: the Leucine Zipper of Nek2 Kinase Exhibits Atypical Conformational Exchange Dynamics. *J Biol Chem* **286**, 27537-27547
34. Xi, Z., Gao, Y., Sirinakis, G., Guo, H., and Zhang, Y. (2012) Single-molecule observation of helix staggering, sliding, and coiled coil misfolding. *Proc Natl Acad of Sci U S A* **109**, 5711-5716

35. Snoberger, A., Brettrager, E. J., and Smith, D. M. (2018) Conformational switching in the coiled-coil domains of a proteasomal ATPase regulates substrate processing. *Nat Commun* **9**, 2374
36. Choi, J., Park, H., and Seok, C. (2011) How Does a Registry Change in Dynein's Coiled-Coil Stalk Drive Binding of Dynein to Microtubules? *Biochemistry* **50**, 7629-7636
37. Kon, T., Imamula, K., Roberts, A. J., Ohkura, R., Knight, P. J., Gibbons, I. R., Burgess, S. A., and Sutoh, K. (2009) Helix sliding in the stalk coiled coil of dynein couples ATPase and microtubule binding. *Nat Struct & Mol Biol* **16**, 325-333
38. Stathopulos, P. B., Schindl, R., Fahrner, M., Zheng, L., Gasmi-Seabrook, G. M., Muik, M., Romanin, C., and Ikura, M. (2013) STIM1/Orai1 coiled-coil interplay in the regulation of store-operated calcium entry. *Nat commun* **4**, 2963-2963
39. Adams, P. D., Afonine, P. V., Bunkoczi, G., Chen, V. B., Davis, I. W., Echols, N., Headd, J. J., Hung, L.-W., Kapral, G. J., Grosse-Kunstleve, R. W., McCoy, A. J., Moriarty, N. W., Oeffner, R., Read, R. J., Richardson, D. C., Richardson, J. S., Terwilliger, T. C., and Zwart, P. H. (2010) PHENIX: a comprehensive Python-based system for macromolecular structure solution. *Acta Crystallogr D* **66**, 213-221
40. Crick, F. (1953) The packing of alpha-helices: simple coiled-coils. *Acta Cryst* **6**, 689-697
41. O'Shea, E., Klemm, J., Kim, P., and Alber, T. (1991) X-ray structure of the GCN4 leucine zipper, a two-stranded, parallel coiled coil. *Science* **254**, 539-544
42. Niethammer, M., Smith, D. S., Ayala, R., Peng, J., Ko, J., Lee, M.-S., Morabito, M., and Tsai, L.-H. (2000) NUDEL Is a Novel Cdk5 Substrate that Associates with LIS1 and Cytoplasmic Dynein. *Neuron* **28**, 697-711
43. Efimov, V. P., and Morris, N. R. (2000) The Lis1-Related Nudf Protein of Aspergillus nidulans Interacts with the Coiled-Coil Domain of the Nude/Ro11 Protein. *J Cell Biol* **150**, 681
44. Stehman, S. A., Chen, Y., McKenney, R. J., and Vallee, R. B. (2007) NudE and NudEL are required for mitotic progression and are involved in dynein recruitment to kinetochores. *J Cell Biol* **178**, 583
45. Olenick, M. A., Dominguez, R., and Holzbaur, E. L. F. (2019) Dynein activator Hook1 is required for trafficking of BDNF-signaling endosomes in neurons. *J Cell Biol* **218**, 220
46. Bielska, E., Schuster, M., Roger, Y., Berepiki, A., Soanes, D. M., Talbot, N. J., and Steinberg, G. (2014) Hook is an adapter that coordinates kinesin-3 and dynein cargo attachment on early endosomes. *J Cell Biol* **204**, 989-1007
47. Cantalupo, G., Alifano, P., Roberti, V., Bruni, C. B., and Bucci, C. (2001) Rab-interacting lysosomal protein (RILP): the Rab7 effector required for transport to lysosomes. *EMBO J* **20**, 683-693
48. Griffis, E. R., Stuurman, N., and Vale, R. D. (2007) Spindly, a novel protein essential for silencing the spindle assembly checkpoint, recruits dynein to the kinetochore. *J Cell Biol* **177**, 1005
49. Mosalaganti, S., Keller, J., Altenfeld, A., Winzker, M., Rombaut, P., Saur, M., Petrovic, A., Wehenkel, A., Wohlgemuth, S., Müller, F., Maffini, S., Bange, T., Herzog, F., Waldmann, H., Raunser, S., and Musacchio, A. (2017) Structure of the RZZ complex and molecular basis of its interaction with Spindly. *J Cell Biol* **216**, 961-981
50. Bianco, A., Dienstbier, M., Salter, H. K., Gatto, G., and Bullock, S. L. (2010) Bicaudal-D Regulates Fragile X Mental Retardation Protein Levels, Motility, and Function during Neuronal Morphogenesis. *Curr Biol* **20**, 1487-1492
51. Emsley, P., Lohkamp, B., Scott, W. G., and Cowtan, K. (2010) Features and development of Coot. *Acta Cryst D* **D66**, 486-501
52. Chen, V. B., Arendall, W. B., Headd, J. J., Keedy, D. A., Immormino, R. M., Kapral, G. J., Murray, L. W., Richardson, J. S., and Richardson, D. C. (2010) MolProbity: all-atom structure validation for macromolecular crystallography. *Acta Crystallogr D Biol Crystallogr* **66**, 12-21
53. Walshaw, J., and Woolfson, D. N. (2001) SOCKET: a program for identifying and analysing coiled-coil motifs within protein structures. *J Mol Biol* **307**, 1427-1450

54. Krissinel, E., and Henrick, K. (2007) Inference of macromolecular assemblies from crystalline state. *J Mol Biol* **372**, 774-797
55. Humphrey, W., Dalke, A., and Schulten, K. (1996) VMD: Visual molecular dynamics. *J Mol Graph* **14**, 33-38
56. Jurrus, E., Engel, D., Star, K., Monson, K., Brandi, J., Felberg, L. E., Brookes, D. H., Wilson, L., Chen, J., Liles, K., Chun, M., Li, P., Gohara, D. W., Dolinsky, T., Konecny, R., Koes, D. R., Nielsen, J. E., Head-Gordon, T., Geng, W., Krasny, R., Wei, G.-W., Holst, M. J., McCammon, J. A., and Baker, N. A. (2018) Improvements to the APBS biomolecular solvation software suite. *Protein Science* **27**, 112-128
57. Case, D. A., Betz, R. M., Cerutti, D. S., Cheatham III, T. E., Darden, T. A., Duke, R. E., Giese, T. J., Gohlke, H., Goetz, A. W., Homeyer, N., Izadi, S., Janowski, P., Kaus, J., Kovalenko, A., Lee, T. S., LeGrand, S., Li, P., Lin, C., Luchko, T., Luo, R., Madej, B., Mermelstein, D., Merz, K. M., Monard, G., Nguyen, H., Nguyen, H. T., Omelyan, I., Onufriev, A., Roe, D. R., Roitberg, A., Sagui, C., Simmerling, C. L., Botello-Smith, W. M., Swails, J., Walker, R. C., Wang, J., Wolf, R. M., Wu, X., Xiao, L., and Kollman, P. A. (2016) AMBER 2016, University of California, San Francisco.
58. Towns, J., Cockerill, T., Dahan, M., Foster, I., Gaither, K., Grimshaw, A., Hazlewood, V., Lathrop, S., Lifka, D., Peterson, G. D., Roskies, R., Scott, J. R., and Wilkins-Diehr, N. (2014) XSEDE: Accelerating Scientific Discovery. *Comput Sci Eng* **16**, 62-74

Table 1 Crystallographic statistics

Data collection statistics	
Space group	$P\ 3_1\ 2\ 1$
Unit cell parameters a, b, c (Å)	60.0, 60.0, 142.6
Unit cell parameters α, β, γ	90°, 90°, 120°
Wavelength (Å)	0.9791
Resolution range (Å)	19.47-2.35 (2.434-2.35)
Total Reflections	125766 (12111)
Unique Reflections	12955 (1263)
Redundancy	9.7 (9.6)
Completeness (%)	99.39 (99.92)
$I/\sigma(I)$	27.98 (1.26)
Wilson B-factor (Å^2)	72.37
R_{merge}	0.0443 (1.621)
R_{meas}	0.04684 (1.713)
R_{pim}	0.01498 (0.549)
CC1/2	1 (0.573)
CC*	1 (0.854)
Refinement statistics	
R_{free} (%)	25.99 (38.38)
R_{work} (%)	25.06 (36.04)
Reflections (work/test sets)	12948/640
R.m.s.d. bonds (Å)/angles	0.005/0.77
Average B-factor (Å^2)	96.46
MolProbity validation	
Ramachandran plot favored	100%
Ramachandran plot allowed	0%
Ramachandran plot outliers	0%
Rotamer outliers	0.85%
Clash score	1.83

The statistics for the high-resolution shell are shown in parenthesis.

Table 2 Numbering of homologous key residues in *Dm* BicD and *Hs* BicD2

	***Dm* BicD**	***Hs* BicD2**
Conversion	Residue *i*	Residue *i*+59
C-terminal domain (CTD)	656-745	715-804
Bicaudal mutant	F684I	F743I
Key aromatic residues	F684, F691, Y698	F743, F750, Y757
Nup358 interface residues*	L687, R688, M690, R694	L746, R747, M749, R753

*Interface residues were mapped for *Ms* BicD1, a close homolog of *Hs* BicD2 (10). Residue *i* of *Hs* BicD2 (as listed in the table) is homologous to residue *i-2* of *Ms* BicD1.

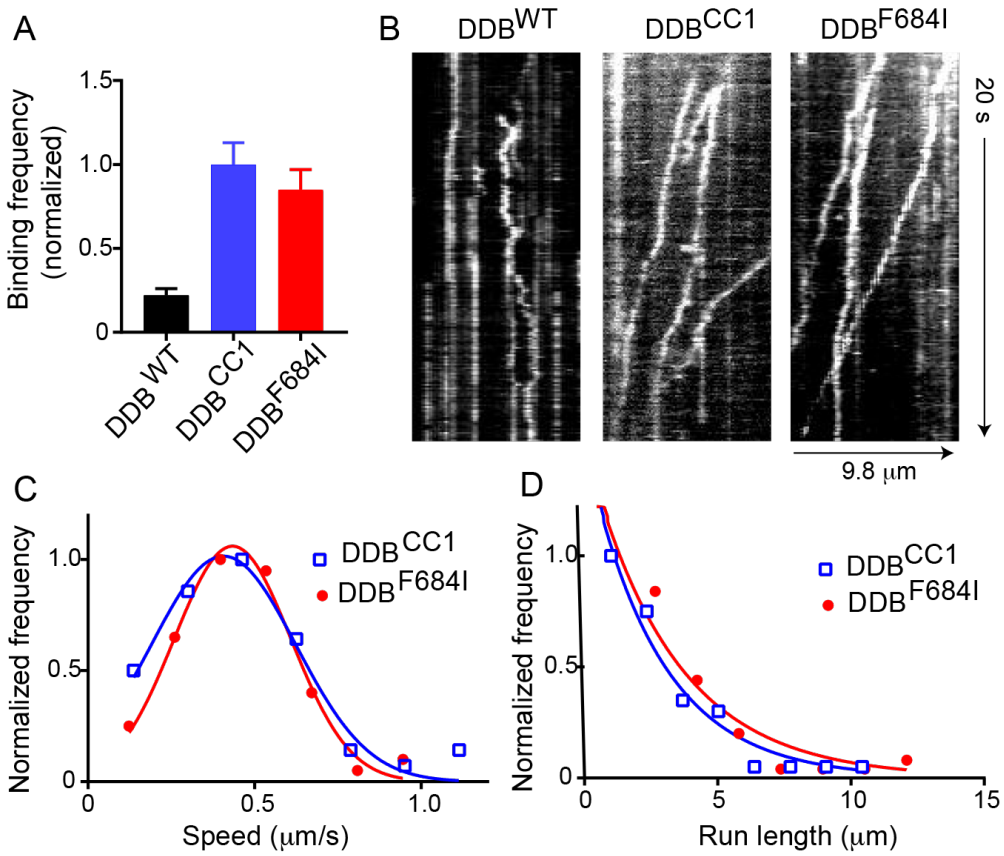

Figure 1. Full-length *Dm* BicD^{F684I} is not auto-inhibited for dynein-dynactin recruitment. (A) Normalized run frequency of dynein-dynactin-BicD (DDB) with different *Dm* BicD mutants: full-length WT BicD (black), truncated BicD-CC1 (blue), and full-length mutant BicD/F684I (red). The binding frequency of DDB^{CC1} is normalized to one. Frequencies of DDB^{CC1} and DDB^{F684I} are 4.5-fold and 3.8-fold higher, respectively, than DDB^{WT}. Motion of DDB^{WT} is mainly diffusive. (B) Kymographs of the three DDB complexes. DDB^{WT} is either static or diffusive, while the other two complexes show processive motion (sloped lines). (C) The speed of DDB^{CC1} (blue) and DDB^{F684I} (red) are 0.41 ± 0.21 μm/s, n=58) and 0.43 ± 0.17 μm/s (n=68) (mean ± SD), respectively, which were not significantly different (p=0.44). (D) Run length of DDB^{CC1} (2.8 ± 0.13 μm, n=58, blue) and DDB^{F684I} (3.3 ± 0.18 μm, n=68, red) (mean ± SD) were not significantly different (p=0.9). Data from 3 independent experiments were pooled.

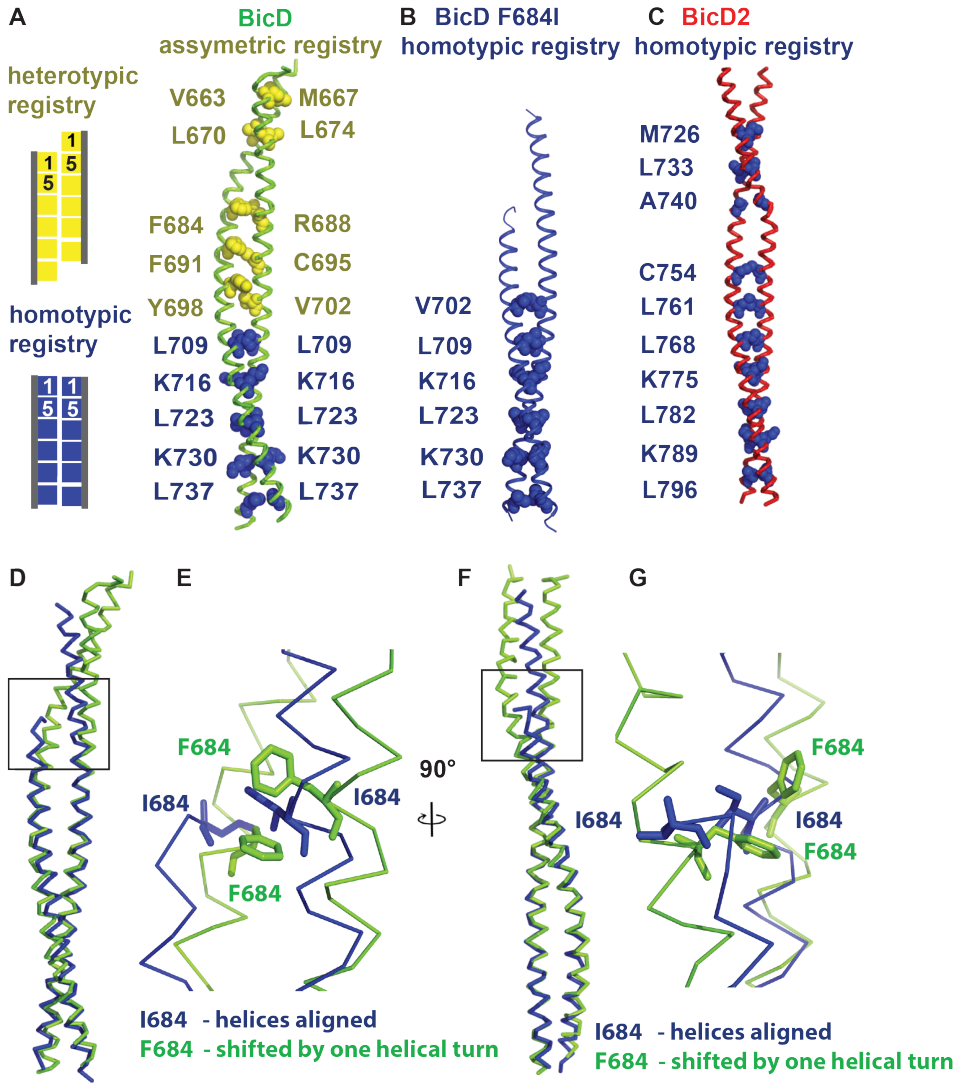

Figure 2 *Dm* BicD-CTD/F684I assumes a conformation with homotypic coiled-coil registry. (A) The structure of *Dm* BicD-CTD wild type (PDB ID 4BL6) (9) which has an asymmetric coiled-coil registry is shown in cartoon representation next to a schematic illustrating coiled-coil registries (left panel). Knob residues in the "a" position of the heptad repeat are shown in spheres representation (heterotypic registry yellow, homotypic registry dark blue). (B) Structure of *Dm* BicD-CTD/F684I, which has a homotypic registry. (C) Structure of *Hs* BicD2-CTD (PDB ID 6OFP) (29), which has a homotypic registry. (D-G) Least squares superimposed structures of the *Dm* BicD-CTD wild type (green) and the F684I mutant (dark blue) are shown as C-α traces, and are rotated by 90° in (D, F). (E, G) Close-up of boxed the boxed area in (D, F). Residues F684 and I684 are shown in stick representation. Note that in the structure of the Bicaudal mutant, the I684 residues from both chains of the dimer are aligned at the same height, consistent with a homotypic registry, while in the wild type structure, the F684 residues from both monomers are vertically shifted by one helical turn respective to each other, consistent with a heterotypic registry.

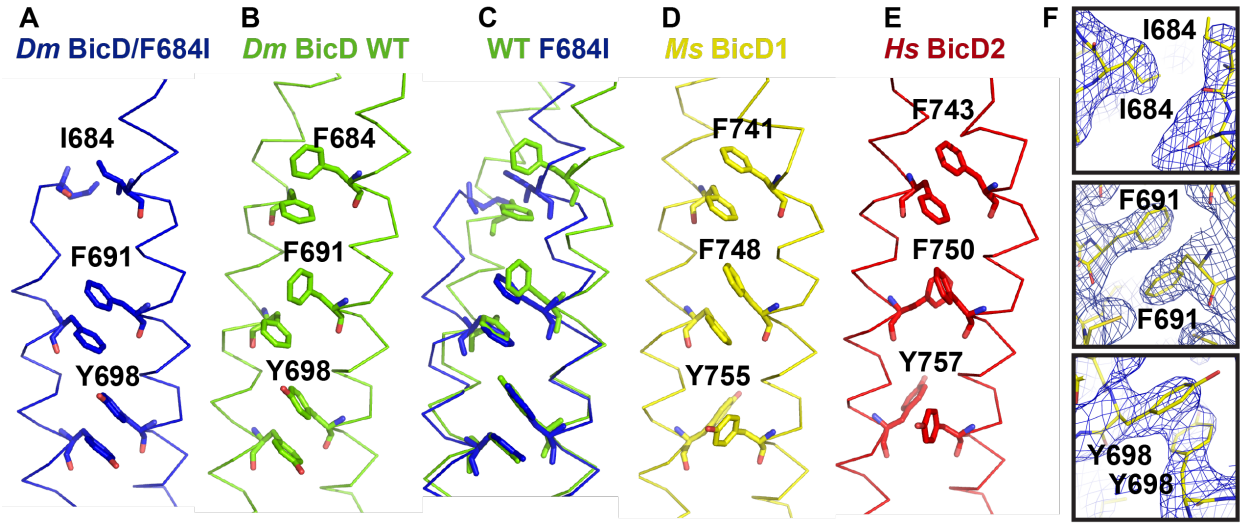

Figure 3. Conformation of key aromatic residues in *Dm* BicD-CTD/F684I. (A) The Cα-trace of the structure of *Dm* BicD-CTD/F684I is shown (blue). Residues I684, F691, Y698 are labeled and shown in stick representation. (B) Structure of the wild type *Dm* BicD-CTD (green, PDB ID 4BL6) (9). (C) Least squares superimposed structures of *Dm* BicD-CTD/F684I and the wild type. (D, E) Structures of the *Dm* BicD homologs (D) *Ms* BicD1-CTD (yellow, PDB ID 4YTD) (10) and (E) *Hs* BicD2-CTD (red, PDB ID 6OFP) (29). (F) Structure of the *Dm* BicD-CTD/F684I mutant in stick representation overlaid with the $2F_O$-F_C electron density map (blue mesh). Close-ups of residues I684, F691 and Y698 are shown in three panels. Note that residues F691 from both chains are oriented face-to-face, as observed in the structures with the homotypic registries.

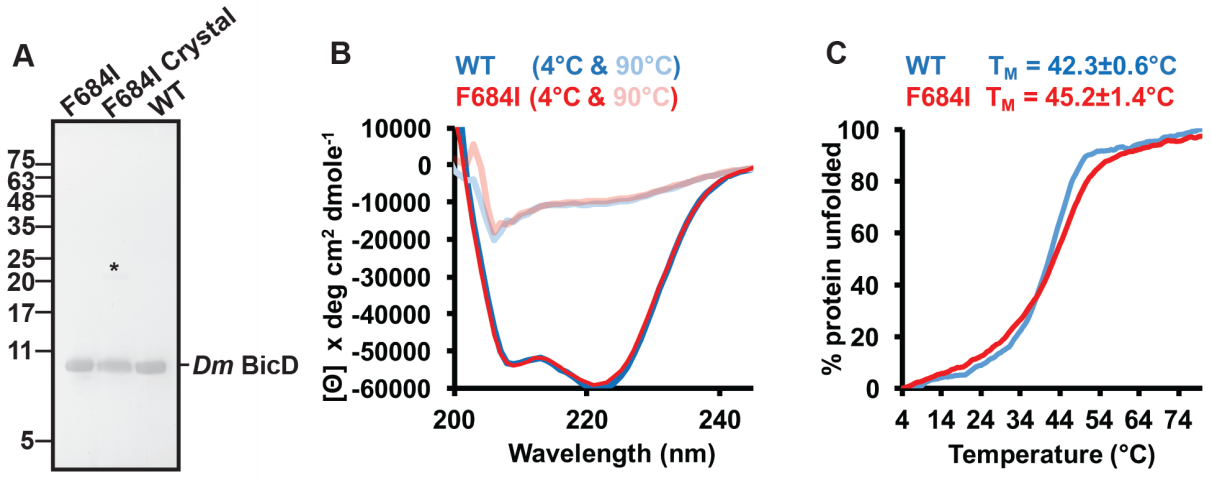

Figure 4 The intact *Dm* BicD-CTD/F684I is present in the crystal and it is fully folded. (A) SDS-PAGE analysis of purified *Dm* BicD-CTD/F684I (left lane), *Dm* BicD-CTD/F684I crystals (middle lane), and purified wild type protein (right lane). The position of the dimer band is indicated by an asterisk. For the crystal sample, 20 crystals were washed three times with reservoir buffer before being dissolved in gel filtration buffer. (B) CD wavelength scans of *Dm* BicD-CTD WT (blue) and *Dm* BicD-CTD/F684I (red) at 4°C (native) and 90°C (random coil). The mean residue molar ellipticity [Θ] versus the wavelength is shown. (C) Thermal unfolding curves of wild type (blue) and F684I (red) were recorded by CD spectroscopy at 222 nm. Molar ellipticity [Θ] versus temperature is plotted. 0% and 100% protein unfolded represent the values of $[\Theta]_{min}$ and $[\Theta]_{max}$, respectively. Melting temperatures T_M of *Dm* BicD-CTD WT and F684I are shown.

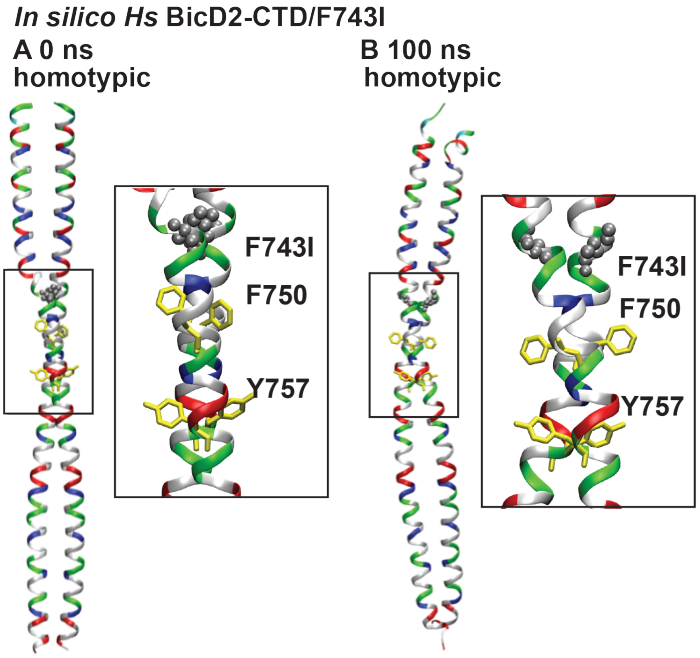

Figure 5 MD simulations suggest that a conformation of the mutant with homotypic registry is stable. (A) Cartoon representation of the crystal structure of human BicD2-CTD (29), with homotypic registry, colored by residue type (blue: positively charged, red: negatively charged, green: polar, white: non-polar). F743 was mutated to isoleucine (silver spheres). F750 and F757 are shown in yellow stick representation. A close-up of the boxed area is shown on the right. (B) Equilibrated structure of the F743I mutant of human BicD2-CTD at the end of a 100 ns MD simulation. Note that the structure maintains a homotypic coiled-coil registry.

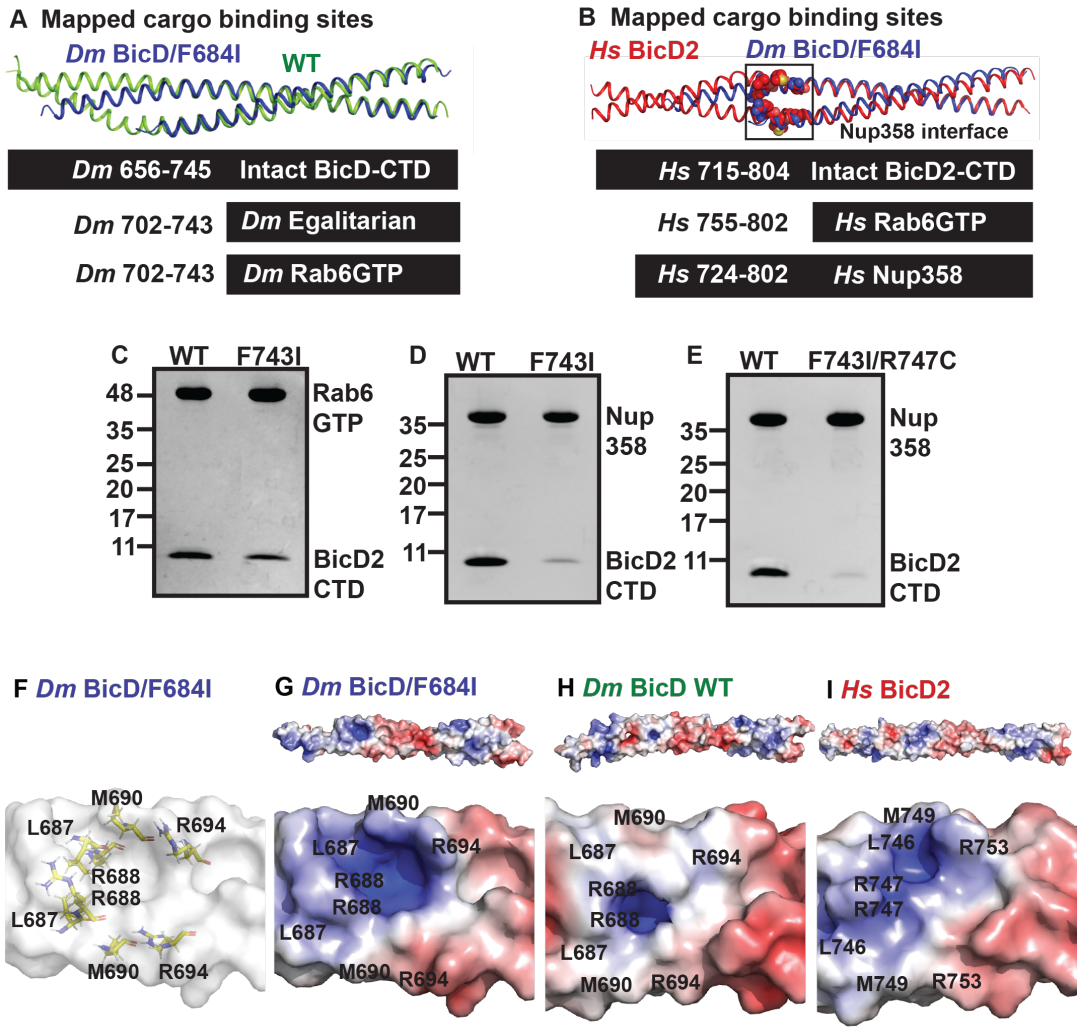

Figure 6. Role of coiled-coil registry shifts in cargo selection of human BicD2. (A) Least-squares superimposition of the structures of *Dm* BicD-CTD/F684I (dark blue) and wild-type (green) in cartoon representation is shown. A schematic representation of the intact *Dm* BicD-CTD (black bar) and of the mapped cargo binding sites including residue numbers is shown below. (B) Least squares superimposition of the structures of *Dm* BicD-CTD/F684I (dark blue) and *Hs* BicD2-CTD (red) in cartoon representation, with a schematic representation of the intact protein and the mapped cargo binding sites below. Known Nup358/BicD2 interface residues (see Table 2) are shown in spheres representation (10). (C-E) Pull-down-assays of BicD2-CTD wild type and its mutants F743I and F743I/R747C with GST-tagged cargoes. An SDS-PAGE of the elution fraction is shown. (C) Rab6^{GTP}-GST and BicD2-CTD wild type or F743I. (D) Nup358-min-GST and BicD2-CTD wild type or F743I. (E) Nup358-min-GST and BicD2-CTD WT or F743I/R747C. (F) Surface representation of the structure of *Dm* BicD-CTD/F684I. Several important Nup358/BicD2 interface residues are known (10) (see Table 2); homologous *Dm* residues are shown in stick representation and labeled. (G-I) The surface electrostatic potential of distinct structures is shown. Positive (blue: 5 kT/e) and negative (red: -5 kT/e) potentials are mapped on the solvent excluded molecular surface (top panel). The bottom panel shows a close-up of the known BicD2/Nup358 interface residues. The same view as in (F) is shown. (G) *Dm* BicD-CTD F684I. (H *Dm* BicD-CTD wild type (9). (I) *Hs* BicD2-CTD (29).